

1 **Elucidating structural order and disorder phenomena in mullite-type $\text{Al}_4\text{B}_2\text{O}_9$ by automated**
2 **electron diffraction tomography**

3 Haishuang Zhao^[1], Yaşar Krysiak^[1], Kristin Hoffmann^[2,3], Bastian Barton^[1], Leopoldo Molina-Luna^[4], Reinhard
4 B. Neder^[5], Hans-Joachim Kleebe^[4], Thorsten M. Gesing^[3,6], Hartmut Schneider^[2], Reinhard X. Fischer^[2,6] and
5 Ute Kolb^{[1]*}

6 [1] Institute of Inorganic Chemistry and Analytical Chemistry, Jakob-Welder-Weg 11, Johannes Gutenberg-
7 University Mainz, 55128 Mainz, Germany

8 [2] Crystallography, Department of Geosciences, Klagenfurter Str. 2, GEO, University of Bremen, 28359
9 Bremen, Germany

10 [3] Institute of Inorganic Chemistry and Crystallography, Leobener Str. NW2, University of Bremen, 28359
11 Bremen, Germany

12 [4] Department of Materials and Geoscience, Technische Universität Darmstadt, Petersenstr. 23, 64287
13 Darmstadt, Germany

14 [5] Department of Physics, Lehrstuhl für Kristallographie und Strukturphysik, Friedrich-Alexander University
15 Erlangen-Nürnberg, Staudtstr. 3, 91058 Erlangen, Germany.

16 [6] MAPEX Center for Materials and Processes, Bibliothekstr. 1, University of Bremen, 28359 Bremen,
17 Germany

18 *Corresponding author: Ute Kolb. Email: kolb@uni-mainz.de; phone: +49 6131 3924154; fax: +49 6131 3923768

19 **Abstract**

20 The crystal structure and disorder phenomena of $\text{Al}_4\text{B}_2\text{O}_9$, an aluminum borate from the mullite-type family,
21 were studied using automated diffraction tomography (ADT), a recently established method for collection and
22 analysis of electron diffraction data. $\text{Al}_4\text{B}_2\text{O}_9$, prepared by sol-gel approach, crystallizes in the monoclinic space
23 group $C2/m$. The *ab initio* structure determination based on three-dimensional electron diffraction data from
24 single ordered crystals reveals that edge-connected AlO_6 octahedra expanding along the **b** axis constitute the
25 backbone. The ordered structure (*A*) was confirmed by TEM and HAADF-STEM images. Furthermore,
26 disordered crystals with diffuse scattering along the **b** axis are observed. Analysis of the modulation pattern
27 implies a mean superstructure (*AAB*) with a threefold **b** axis, where *B* corresponds to an *A* layer shifted by $\frac{1}{2}\mathbf{a}$
28 and $\frac{1}{2}\mathbf{c}$. Diffraction patterns simulated for the *AAB* sequence including additional stacking disorder are in good
29 agreement with experimental electron diffraction patterns.

30 **Key words**

31 Electron diffraction; Aluminum borate; Crystal structure determination; Superstructure; Disorder

32 **Introduction**

33 One-dimensional structures, such as nanowires, nanotubes, and nanobelts, gained considerable attention in
34 material research and solid-state chemistry due to their potential applications [1] in electronics, optics and
35 mechanics. Aluminum borate nanorods are important mullite-type ceramic raw materials with high temperature
36 stability, low temperature expansion, excellent mechanical properties and corrosion resistance [2–5]. The most
37 frequently investigated aluminum borates in the $\text{Al}_2\text{O}_3\text{-B}_2\text{O}_3$ system include $\text{Al}_{18}\text{B}_4\text{O}_{33}$ ($9\text{Al}_2\text{O}_3\text{:}2\text{B}_2\text{O}_3$), Al_5BO_9
38 ($5\text{Al}_2\text{O}_3\text{:B}_2\text{O}_3$) and $\text{Al}_4\text{B}_2\text{O}_9$ ($2\text{Al}_2\text{O}_3\text{:B}_2\text{O}_3$) [6,7]. Mullite-type aluminum borates can be prepared by solid-state
39 reaction at high temperature [2,6]. In addition, other approaches, such as sol-gel synthesis, one-step combustion
40 method, and thermal evaporation, have been applied to improve the formation and properties [3,7,8]. One of the
41 characteristic properties of mullite-type structures are linear edge-sharing octahedral chains, which are connected
42 parallel to each other by different inter-chain units controlling the growth of nanowires and nanorods [4,9].
43 Threefold and fourfold coordinated B atoms in the inter-chain units increase complexity, and disorder
44 phenomena can be often observed in mullite-type structures.

45 $\text{Al}_4\text{B}_2\text{O}_9$ shows a structure similar to boralsilite ($\text{Al}_{16}\text{B}_6\text{Si}_2\text{O}_{37}$) [10]. The structure of $\text{Al}_4\text{B}_2\text{O}_9$ was first
46 investigated by Scholze *et al.* [11]. An orthorhombic lattice was proposed by the author with $a = 14.8(2)$ Å, $b =$
47 $15.1(2)$ Å, $c = 5.6(1)$ Å, and $Z = 8$, with reflection conditions indicating space groups $Cmm2$, $Cm2m$, $C222$, or
48 $Cmmm$. Mazza *et al.* [12] described the structure of a metastable analogue with similar composition in space
49 group $Pbam$ with a pseudo tetragonal symmetry. Fischer *et al.* [7] investigated the crystal structure of $\text{Al}_4\text{B}_2\text{O}_9$
50 using a combination of NMR spectroscopy and X-ray powder diffraction. The structure was determined to have
51 a monoclinic unit cell in space group $C2/m$ close to the orthorhombic lattice. The initial structure was derived
52 based on the closely related boralsilite structure and refined with Rietveld methods from X-ray powder
53 diffraction data. Similar results were obtained from neutron diffraction data [13]. However, some crystal-
54 chemical details like the positions of two oxygen atoms (O5 and O10) remained unclear not being resolvable by
55 powder diffraction methods for such a complex structure with disordered O atoms. On the other hand, the
56 achievable crystal size was not suitable for single crystal X-ray diffraction. Additional methods must be applied
57 to explain the discrepancies in X-ray and neutron powder-diffraction analyses, and to find a solution for the
58 structural deficiencies of this important aluminum borate. It was shown by electron diffraction methods that
59 structural details vary inside the crystallites, presenting domains with an ordered distribution of the atoms and
60 other domains with a probable disordered configuration of the oxygen atoms as discussed here in more detail.

61 In this work, transmission electron microscopy (TEM) was used to elucidate the crystal structure of $\text{Al}_4\text{B}_2\text{O}_9$,
62 providing structural and chemical information. In addition, high-resolution imaging yields atomically resolved
63 projection images. Electron diffraction, as opposed to X-ray powder diffraction, is able to provide atomic
64 structure information from a single nanocrystal. It has advantages over X-ray powder diffraction in the case of
65 structures with large unit-cells, low symmetry, superstructures, low crystallinity, as well as for samples with
66 impurities or multiple phases. Three-dimensional electron diffraction data with reduced dynamical scattering can
67 be acquired from a single crystalline crystal through sequential tilt series using the recently developed automated
68 electron diffraction tomography (ADT) method [14,15]. Electron beam precession may be combined during data
69 acquisition, providing a full integration of the reciprocal space thus improving reflection intensities. In recent
70 years, a number of *ab initio* structure solutions were successfully performed based on ADT datasets for materials

71 including nano crystalline phases such as single inorganic nanoparticles, as well as beam-sensitive organic
72 nanocrystals [16,17].

73 **Experimental**

74 **Sample synthesis**

75 $\text{Al}_4\text{B}_2\text{O}_9$ was synthesized using the nitrate decomposition method as described previously [7,12,13,18], with an
76 initial composition of 35 wt% Al_2O_3 and 65 wt% B_2O_3 . Aluminum nitrate nonahydrate $\text{Al}(\text{NO}_3)_3 \cdot 9\text{H}_2\text{O}$ and boric
77 acid $\text{B}(\text{OH})_3$ were mixed and dissolved in 10 wt.% glycerol. The resulting foam was dried, crushed into powder
78 and finally crystallized at 1223 K for 44 hours, using covered platinum crucibles. The sample was quenched to
79 room temperature and washed with hot deionized water to remove possible impurities of boric acid, which was
80 used with an excess during the synthesis.

81 **X-ray powder diffraction**

82 Powder X-ray diffraction data was measured on a Philips X'Pert diffractometer using $\text{CuK}\alpha$ radiation and Bragg-
83 Brentano geometry. In the primary beam the instrument is equipped with an 0.25° divergence slit, an 0.5° anti
84 scatter slit, a soller slit (0.04 rad) and a mask (10 mm), as well as a soller slit (0.04 rad), a Ni-filter and a
85 X'Celerator detector system in the secondary beam. X-ray diffraction data was collected from 3° to 120° in
86 2θ with a step size of 0.0167° , a measuring time of 50 seconds per step, and tube settings of 45kV and 40mA. A
87 Pawley fit was carried out with the program *TOPAS-Academic* [19].

88 **TEM sample preparation**

89 A small quantity of the powder was ground and dispersed in ethanol using an ultrasonic bath. The suspension
90 was transferred into a caved tip with a pipette and then sprayed onto a thin amorphous carbon film, suspended on
91 standard 300 mesh Cu TEM grids, using an ultrasonic vaporizer [20]. The grid was dried under vacuum and
92 cleaned in argon plasma for 20 s before it was transferred into the TEM column.

93 **STEM, HRTEM, EDX and ADT**

94 Phase contrast TEM, scanning TEM (STEM), energy-dispersive X-ray spectroscopy (EDX), and automated
95 diffraction tomography (ADT) measurements were carried out using a TECNAI F30 S-TWIN transmission
96 electron microscope equipped with a field emission gun and operating at 300 kV. STEM images were collected
97 using a Fischione high-angle annular dark field (HAADF) detector. TEM images and nano electron diffraction
98 (NED) patterns were acquired with a 4k x 4k Gatan US4000 CCD camera (Gatan, Pleasanton, USA). EDX
99 spectra were taken with an Oxford EDAX EDX spectrometer, equipped with a Si/Li detector with an ultrathin
100 window.

101 Electron diffraction data were collected at room temperature with an automated acquisition module developed
102 for FEI microscopes [14]. A Fischione dual-axis tomography holder (Model 2040) with a tilt range of at least \pm
103 60° was used for electron diffraction data acquisition. A small condenser aperture of 10 μm , weak gun lens and

104 large condenser spot size were used in order to reduce the electron dose rate to about $10 \text{ e}^-/\text{\AA}^2\text{s}$ on the sample.
105 The crystal position was tracked in microprobe STEM mode, and electron diffraction patterns were collected
106 using the above settings. The beam size was set to 75 nm in diameter. In order to reduce dynamic effects and
107 improve the reflection intensity integration, ADT was coupled with precession electron diffraction (PED) [20,21],
108 which was performed using a NanoMEGAS DigStar unit. The precession angle of the beam was kept at 1° .
109 Several ADT tilt series were collected sequentially in a fixed tilt step of 1° . The exposure time for each frame
110 was set to 4 seconds. The NED data without electron beam precession were used for accurate cell parameter
111 determination and extinction symbol analysis.

112 Aberration-corrected High Angle Annular Dark Field (HAADF-STEM) images were acquired using a probe-
113 corrected JEM-ARM200F equipped with a Schottky emitter and operated at 200 kV, with a 0.08 nm probe, 22
114 mrad convergence and HAADF angles of 90 - 370 mrad. For high resolution imaging the samples were drop-cast
115 on copper grids covered with a holey amorphous carbon film. Images were acquired using the DigitalMicrograph
116 software. The atomic resolution HAADF-STEM images were processed using Fourier filtering to reduce noise.
117 HAADF-STEM image simulation was carried out using the *QSTEM* software [22].

118 TEM in-line holography was realized by focal series reconstruction from image series recorded using the FEI
119 F30 ST as described above, without aberration corrector, under suitable high-resolution TEM conditions. 20
120 images were recorded at a primary magnification of 790,000 with 6 nm focal increment, thus covering a focal
121 range of 114 nm including Gaussian focus. The accumulated dose per focal series was about $21,000 \text{ e}^-/\text{\AA}^2$. The
122 images were hardware-binned by 2, followed by an additional software binning by 2 resulting in $1\text{k} \times 1\text{k}$ images
123 with a physical pixel size of 0.0576 nm. After image alignment, a 350^2 pixel region was chosen for exit wave
124 reconstruction, employing a Gerchberg-Saxton algorithm written using Python. Residual axial aberrations were
125 corrected by an automated minimization routine also implemented in Python [23]. Simulated TEM exit waves
126 were generated using a multislice algorithm included in the *Dr. Probe* software package [24].

127 **Structure solution and refinement**

128 The ADT3D software [15,20] was used for processing the three-dimensional electron diffraction data yielding
129 unit-cell parameters, space group and reflection intensities. The unit-cell parameters were refined with a Pawley
130 fit against XRPD data. The *ab initio* structure solution using direct methods approach implemented in *SIR2014*
131 [25] and Least-squares refinement with the program *SHELX97* [26] were based on the reflection intensities
132 derived from electron diffraction. The crystal structure and models are illustrated with the program *VESTA* [27].

133 **Superstructure simulation**

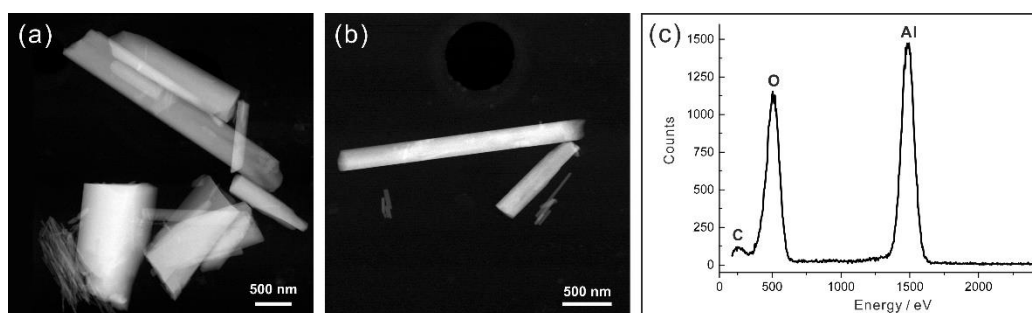
134 In order to simulate diffuse scattering from *AAB·AAB·AAB* sequences with stacking faults, superstructures were
135 modelled and corresponding electron diffraction patterns were calculated with the *DISCUS* software package
136 [28]. The *ac* plane of the ordered structure of $\text{Al}_4\text{B}_2\text{O}_9$ was used as a layer *A*. The *B* layer was created by shifting
137 the *A* layer by $\frac{1}{2}\mathbf{a}$ and $\frac{1}{2}\mathbf{c}$. To simulate the approximately tripled superstructure, an imperfect sequence of layers
138 *A* and *B* was created *via* a Monte Carlo approach. The sequence consisted of double layers *AA* and single *B*
139 layers. *A* predominantly alternating sequence of these double layers *AA* and the single layer *B* results in a

140 sequence like $\cdots ABAABAABAAAABAABBAA \cdots$. The lack of strict periodicity of these triple layer packages
 141 causes broad diffuse maxima at approximately $b^*/3$. The diffraction pattern of a disordered layered structure can
 142 be calculated along two different schemes. In the first scheme, explicit atom coordinates for all atoms in all
 143 layers are calculated according to the stacking sequence of the corresponding layers. This results in a list of atom
 144 coordinates for the full crystal, and the diffraction pattern is calculated by an explicit calculation of the term
 145 $I(hkl) = (\sum_j^N f_j e^{2\pi i (hx_j + ky_j + lz_j)})^2$. In contrast to the structure factor for Bragg scattering the sum includes not
 146 only the atoms in a single unit cell but all atoms within the crystal. As this will be a large number, the second
 147 scheme allows a much faster calculation. A layered structure can be created by a convolution product of the atom
 148 positions within a single layer type with the list of the layer positions. Using the convolution theorem, the
 149 diffraction pattern is the Fourier transform of this convolution product i.e. the regular product of the individual
 150 Fourier transforms. Thus it is sufficient to simulate the atom positions within just a single layer as well as the list
 151 of layer positions. These individual Fourier transforms take much less time to calculate than the Fourier
 152 transform of the full crystal. If several layer types are involved, an outer sum over all layer types is sufficient to
 153 fully describe the disordered layered structure. In our simulations the second scheme was used as coded within
 154 *DISCUS*. The individual layers were simulated as a 10×10 supercell. 200 of these layers were stacked along
 155 the b direction.

156 Results and Discussion

157 TEM overview and EDX analysis

158 Synthetic $\text{Al}_4\text{B}_2\text{O}_9$ sample contains nanorods with different sizes as well as bundles of small rods as shown in
 159 Fig. 1. The rod diameter ranges from a few tens to some hundred nanometers (Fig. 1a and 1b), which is suitable
 160 for TEM investigation. The crystals were stable under mild intensity conditions in the TEM. Electron diffraction
 161 experiments prove that most crystals grow with an ordered structure, while for some crystals the diffraction
 162 patterns exhibited modulated streaks. EDX spectral quantification (Fig. 1c) resulted in an Al:O ratio of 1:2.33,
 163 which is close to the expected ratio of 1:2.25 in $\text{Al}_4\text{B}_2\text{O}_9$.

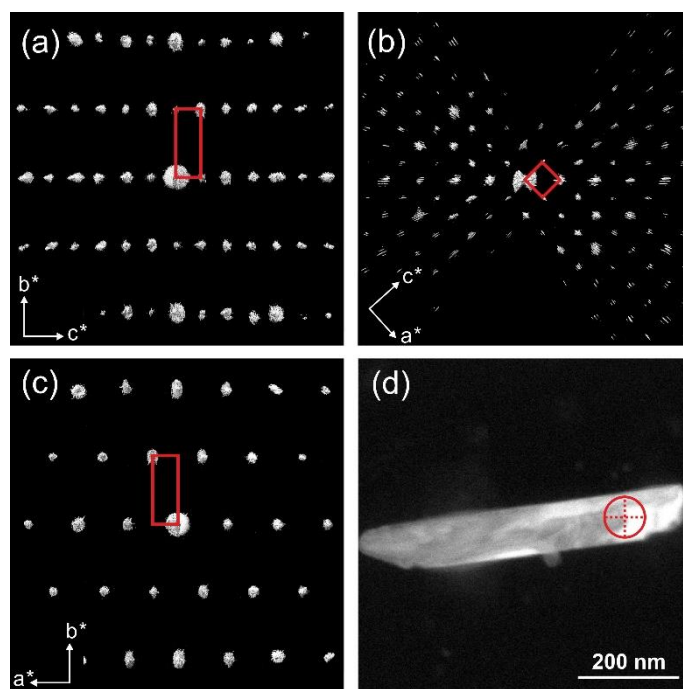


164
 165 Fig. 1 STEM images and EDX spectrum of $\text{Al}_4\text{B}_2\text{O}_9$: (a) overview of nanorods; (b) single separate nanorods; (c)
 166 EDX spectrum of $\text{Al}_4\text{B}_2\text{O}_9$.

167 ADT analysis and structure determination

168 In order to have an unbiased structure determination, we have reevaluated the crystal structure by *ab initio*
 169 structure solution methods based on ADT data taken in NED mode. Eight ADT datasets collected from different

170 crystals were reconstructed in 3D reciprocal volumes (Fig. 2). All data sets yielded *C*-centred unit-cells. Those
 171 acquired without using PED were used for cell parameter determination leading to mean values of $a = 14.73 \text{ \AA}$, b
 172 $= 5.54 \text{ \AA}$, $c = 15.14 \text{ \AA}$, $\alpha = 89.9^\circ$, $\beta = 90.9^\circ$ and $\gamma = 90.3^\circ$ (see Table S1) with deviations of approximately 1% for
 173 crystal axes and 1° for angles. ADT data sets, acquired with PED, without diffuse scattering were selected for
 174 structure solution. As the β is 90° within the error margins, the unit-with cell can be orthorhombic or monoclinic
 175 (pseudo orthorhombic). Systematic extinction with $h + k = 2n$ for hkl reflections indicated a *C*-centred Bravais
 176 lattice. In all three major zones $0kl$ ($k = 2n$), $h0l$ ($h = 2n$), $hk0$ ($h + k = 2n$), shown in Fig. S1 as slices cut from
 177 3D volume, no additional extinction was observed. For the orthorhombic setting, the resulting extinction symbol
 178 was determined as $C - - -$, associated with possible space groups $C222$ (No. 21), $Cmm2$ (No. 35), $Cm2m$ (No.
 179 38), $C2mm$ (No. 38) and $Cmmm$ (No. 65). However, no chemical meaningful structure solution could be
 180 obtained in any of these space groups. Thus, a symmetry reduction into the monoclinic lattice with a
 181 corresponding extinction symbol $C1-1$, consistent with space groups $C2$ (No. 5), Cm (No. 8) and $C2/m$ (No. 12),
 182 was performed. In order to achieve a higher accuracy, the cell parameters were refined by Pawley fit of XRPD
 183 data as $a = 14.8130(10) \text{ \AA}$, $b = 5.5418(3) \text{ \AA}$, $c = 15.0593(9) \text{ \AA}$, $\beta = 90.930(2)^\circ$ and $V = 1236.07(13)$ (Fig. S2),
 184 supporting the monoclinic cell metric, and used for structure solution and refinement based on ADT data.



185

186 Fig. 2 Reconstructed three-dimensional diffraction volume of $\text{Al}_4\text{B}_2\text{O}_9$ obtained by ADT, viewed along the main
 187 directions \mathbf{a}^* , \mathbf{b}^* , \mathbf{c}^* (a, b and c), and STEM image of a single crystal selected for acquisition of the NED data
 188 (d). The beam position for ADT data collection is marked with a red circle in (d).

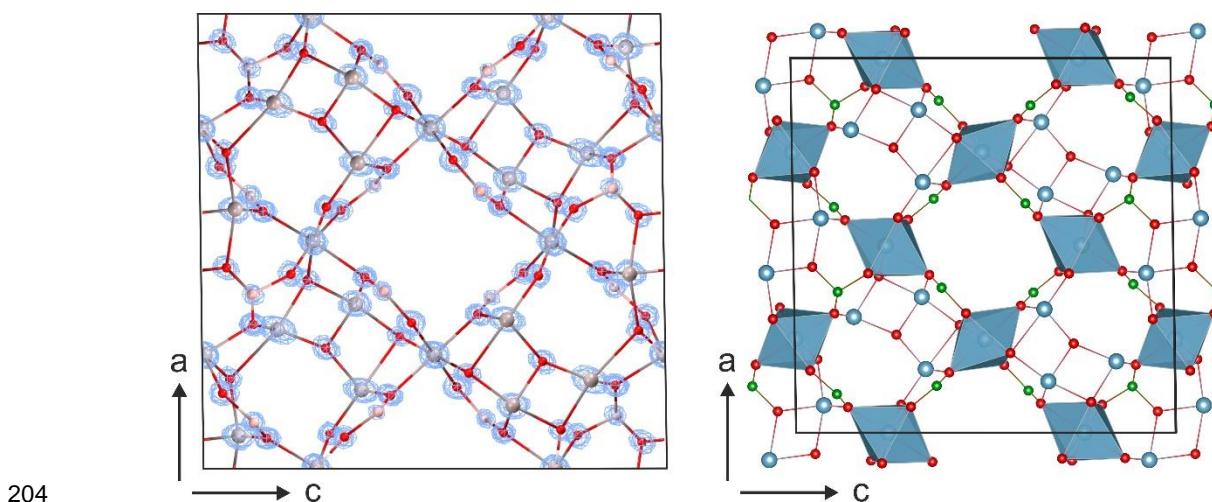
189 Table 1 Experimental parameters of datasets used for structure solution in space group $C2/m$.

dataset	I + II	I	II
Tilt range* ($^\circ$)	136 + 141	-66/+69	-70/+70
No. of total reflections	9475	7009	7312
No. of independent reflections	3035	2251	2647
Resolution (\AA)	0.6	0.6	0.6

190	Independent reflection coverage (%)	94	70	82
	R_{int}	0.169	0.142	0.225
	Overall U (Å)	0.013	0.094	0.093
	Residual R	0.273	0.259	0.293

191 * Data sets obtained merging two ADT data collections with an orthogonal tilt axes from one single crystal.

192 Two ADT acquisitions, sequentially performed from the same crystal with a rotation of the crystal in plane of
 193 about 90° for dataset II (Table 1) were used for crystal structure solution with direct methods in space group
 194 $C2/m$. Each of the two data sets delivers all Al positions while O and B atoms are partly missing. In order to
 195 increase the coverage of independent reflections both ADT acquisitions were merged with scale factor 1. The
 196 resulting data set with improved hkl -completeness was used also for *ab initio* structure solution delivering well
 197 resolved potential maps of the mullite-type structure (Fig. 3). All atoms of the structure could clearly be found in
 198 the model. Seven strong maxima were observed (from 4.9 to 3.0 $e/\text{Å}^3$), corresponding to the seven independent
 199 Al atoms. The next peaks belong to fourteen O atoms found in a scattering potential range of 3.1 down to 1.9 e
 200 $/\text{Å}^3$. The maxima consistent with four independent B atoms detected with a height of 2.3 $e/\text{Å}^3$, 1.8 $e/\text{Å}^3$, 1.6 e
 201 $/\text{Å}^3$ and 1.6 $e/\text{Å}^3$, respectively followed by a residual potential of 0.8 $e/\text{Å}^3$. No extra potential describing an
 202 additional O position was detected. The final structural composition was determined as $\text{Al}_4\text{B}_2\text{O}_9$, which agrees
 203 with the expected synthetic stoichiometry.



204

205 Fig. 3 Left: Potential map of $\text{Al}_4\text{B}_2\text{O}_9$ derived from ADT data overlaid with the reconstructed atomic model,
 206 viewed in (010) direction. Right: refined crystal structure along the same direction exhibiting the monoclinic
 207 angle of 90.93°, Al: light blue, O: red, B: green.

208 The least-squares refinement was performed by SHELX97 using soft geometrical constraints and restraints
 209 converging to a final residual R_1 of 0.36. The structure stayed stable with regular coordinated polyhedra for the
 210 Al atoms and reasonable geometries of tetrahedral BO_4 and trigonal planar BO_3 groups (Table 2) Al5, Al6 and
 211 Al7 are respectively coordinated with six O atoms to form AlO_6 octahedra, which are edge-linked to build linear
 212 octahedral chains running along the b axis. The chains are linked by AlO_5 (or AlO_4), BO_4 and BO_3 groups. The
 213 atomic positions in the structures refined from ADT data and XRPD data [7]; listed in Table S2, show an
 214 excellent agreement. The mean deviations for Al, O and B atoms (0.005 Å, 0.011 Å, 0.013 Å, see Table S3). In
 215 the ADT structure the four-fold coordinated B2 atom connected to O10 shows the largest positional deviation

216 (0.0240 Å) but an improved geometry. The splitting of the oxygen positions (O5 and O10) found in XRPD
217 refinement could not be observed in the ADT structure where the O10 position is fully occupied but no O5
218 position was found.

219

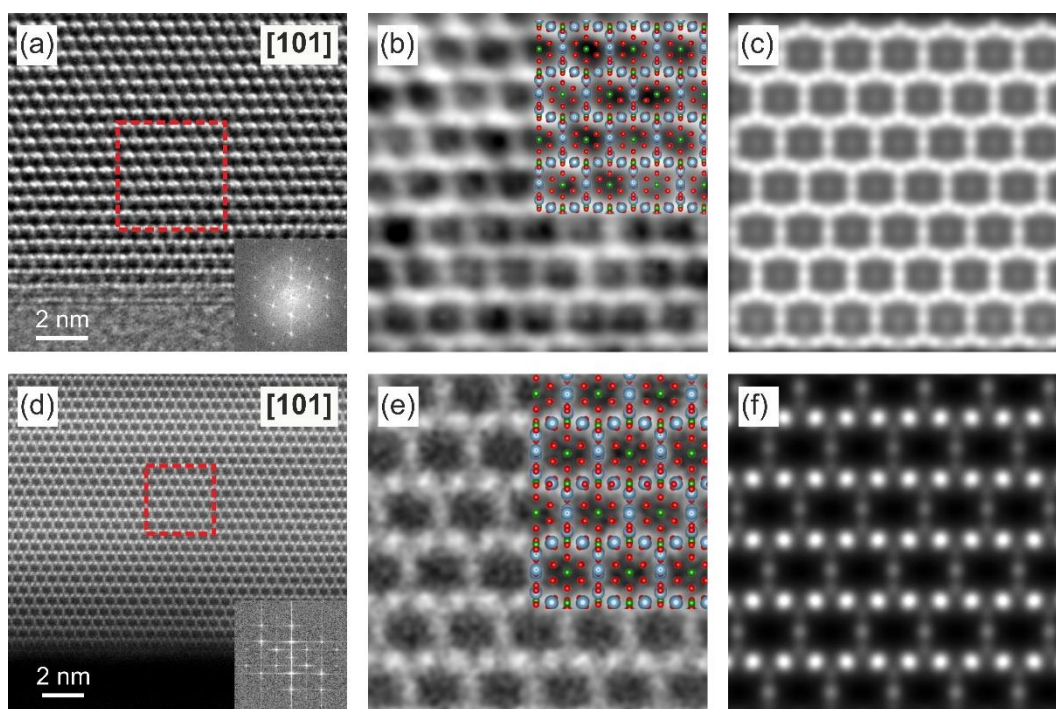
220 Table 2 Selected bond distances (Å) and angles (°) in the $Al_4B_2O_9$ structure refined from ADT data (first column)
 221 and XRPD data [7] (second column with grey background).

AlO_6 octahedra								
Al5—O3	1.906(15)	1.856(14)	Al6—O7	2x1.869(12)	2x1.866(9)	Al7—O2	2x1.799(1)	2x1.772(10)
Al5—O4	2.092(14)	1.984(12)	Al6—O8	2x1.824(12)	2x1.903(10)	Al7—O6	2x1.882(9)	2x1.875(11)
Al5—O9	1.903(15)	2.032(12)	Al6—O15	2x1.957(12)	2x1.895(10)	Al7—O11	2x1.941(14)	2x1.937(8)
Al5—O12	1.796(13)	1.819(14)						
Al5—O13	1.874(12)	1.820(13)						
Al5—O14	1.966(15)	1.8248(13)						
Mean	1.923	1.889		1.883	1.888		1.874	1.861
AlO_5 bi-pyramids or AlO_4 groups								
Al1—O1	1.799(23)	2.017(19)	Al2—O1	1.830(23)	1.668(19)	Al3—O8	1.844(24)	1.882(20)
Al1—O2	1.874(23)	1.847(17)	Al2—O3	1.891(25)	1.801(19)	Al3—O9	2x1.813(12)	2x1.782(12)
Al1—O3	1.884(22)	2.112(15)	Al2—O7	2x1.815(8)	2x1.835(11)	Al3—O10	1.840(26)	1.730(30)
Al1—O4	2x1.846(8)	2x1.813(11)	Al2—O8	2.211(23)	2.231(18)	Al3—O10	1.956(25)	2.084(30)
Mean	1.850	1.920		1.912	1.874		1.853	1.883
For AlO_4				1.838	1.785		1.863	1.794
Al4—O1	1.789(25)	1.813(20)						
Al4—O2	2.198(25)	2.361(0)						
Al4—O11	2x1.827(12)	2x1.760(11)						
Al4—O12	1.716(23)	1.759(19)						
Mean	1.871	1.891						
For AlO_4	1.883	1.773						
BO_3 triangles and BO_4 tetraedra								
B1—O9	2x1.412(13)	2x 1.43(2)	B2—O7	2x1.430(15)	2x 1.55(2)	B3—O11	2x1.411(8)	2x 1.39(2)
B1—O15	1.411(29)	1.43(3)	B2—O10	1.414(29)	1.57(4)	B3—O14	1.316(19)	1.51(4)
			B2—O13	1.406(26)	1.23(3)			
Mean	1.41	1.43		1.42	1.48		1.38	1.43
B4—O4	2x1.372(14)	1.48(2)						
B4—O6	1.396(29)	1.32(3)						
Mean	1.38	1.43						
Selected angles in BO_3 and BO_4 groups								
O9—B1—O15	2x118.6(2)	2x117.7(4)			O7—B2—O10	110.5(2)	85.3(0)	
O9—B1—O9	122.2(1)	124.5(7)			O13—B2—O7	113.3(2)	128.0(0)	
					O13—B2—O10	104.2(2)	107.6(10)	
					O7—B2—O7	105.2(1)	102.6(0)	
O11—B3—O14	2x120.8(2)	2x120.3(3)			O4—B4—O6	2x121.1(1)	2x124.5(4)	
O11—B3—O11	117.7(1)	118.4(6)			O4—B4—O4	117.9(1)	108.2(6)	

222
223

224 **HRTEM and HAADF-HRSTEM**

225 In order to study the ordered structure, high-resolution image methods were used to observe the atomic
 226 information. Fig. 4 compares high resolution TEM holography to HAADF-STEM imaging for $\text{Al}_4\text{B}_2\text{O}_9$ nanorods
 227 viewed along [101]. It can be seen that the structure model solved by ADT is in good agreement with both the
 228 experimental TEM hologram and the HAADF-STEM image (Fig. 4b and Fig. 4e). The main framework is built
 229 up by the O and Al columns. In the TEM hologram phase images, one B column (B1 and B4) surrounded by six
 230 O columns (2xO9, 2xO4, O15 and O6) can be observed in the middle of quasi six rings as a single phase peak.
 231 In the HAADF-STEM images, Al columns produce a larger intensity as compared to O and B, as expected from
 232 the Z-dependence of HAADF-STEM contrast. The ADT structure was used to perform multislice-simulations of
 233 both TEM exit waves and HAADF-STEM images. The simulations are in good agreement to the experimental
 234 images (Fig. 4c and Fig. 4f), confirming the crystal structure solved from ADT data. A STEM overview image is
 235 shown in (Fig. S3).

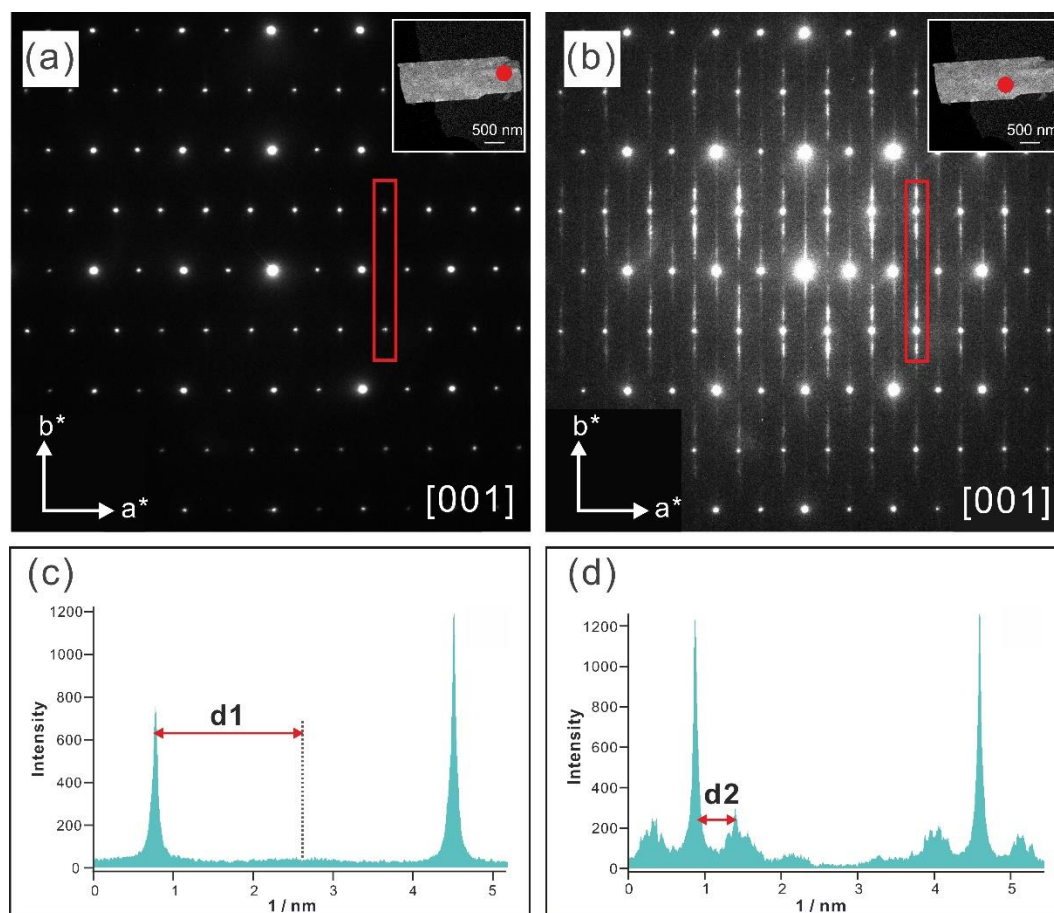


236
 237 Fig. 4 (a) HRTEM image of $\text{Al}_4\text{B}_2\text{O}_9$ recorded along [101] zone axis and squared modulus of the 2D Fourier
 238 transform (power spectrum). (b) Enlarged phase image from the boxed area in (a), overlaid by the $\text{Al}_4\text{B}_2\text{O}_9$ ADT
 239 structure model viewed along [101] (blue: Al, red: O, green: B). (c) Phase of simulated 300 kV exit wave
 240 produced by the ADT structure along [101] direction. (d) HAADF-HRSTEM image of $\text{Al}_4\text{B}_2\text{O}_9$ recorded along
 241 [101] zone axis with related power spectrum. (e) Enlarged image from the selected area of (d) with $\text{Al}_4\text{B}_2\text{O}_9$
 242 structure model viewed along the [010] direction. (f) Simulated HAADF-HRTEM of $\text{Al}_4\text{B}_2\text{O}_9$ viewed along [101]
 243 zone axis.

244

245 **Disorder analysis and simulation**

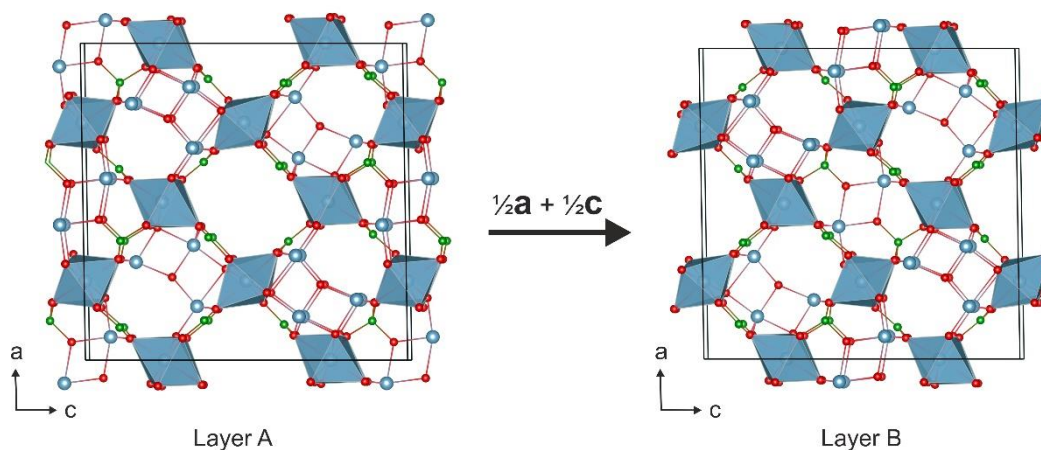
246 Subsequent to the structural analysis performed on ordered single nano crystals the focus was set onto additional
 247 diffraction intensities observed for some of the investigated crystals. Fig. 5 presents electron nano diffraction
 248 patterns both showing the [001] zone taken from two different regions of an identical nanorod. Based on the
 249 pattern in Fig. 5a where no superstructure reflections nor diffuse scattering but discrete reflections are observed
 250 an ordered crystal can be assumed. As shown in Fig. 5b, diffraction on a different region of the same crystal,
 251 however, delivers strong and modulated diffuse streaks that run parallel to \mathbf{b}^* . Analysis of the three dimensional
 252 reconstructed reciprocal space did prove that these are indeed one-dimensional streaks. Fig. 5c and 5d show the
 253 intensity profiles between Bragg reflections 510 and $5\bar{1}0$ for the well ordered and disordered regions of the
 254 crystal. In Fig. 5c no significant diffuse scattering is observed between reflections 510 and $5\bar{1}0$. In Fig. 5d broad
 255 diffuse peaks are observed at approximately $51\frac{1}{2}$. This indicates a predominantly three-fold superstructure in
 256 direct space along the \mathbf{b} axis.



257
 258 Fig. 5 (a, b) Single electron nano diffraction patterns recorded from different regions of a $\text{Al}_4\text{B}_2\text{O}_9$ crystallite
 259 oriented in [001] direction, as marked in the STEM insets on the upper right. (a) Highly ordered region. (b)
 260 Disordered area giving rise to modulated streaking in the pattern. (c) and (d): Intensity profiles taken along
 261 corresponding diffraction lines marked in (a) and (b) by red rectangles.

262 As the observed diffuse scattering is rod like in reciprocal space the disorder in direct space must be a stacking
 263 sequence along the \mathbf{b} axis that deviates from the perfect stacking sequence of the average structure. Note that the
 264 $0k0$ rod does not show significant diffuse scattering, see the reconstructed pattern in Fig. 7a as well. The weak
 265 diffuse streaks along \mathbf{b}^* at the $0k0$ rod and through reflections $h00$ with h even is not modulated but decreases

266 monotonically away from reflection positions at k integer (Fig. S4). This weaker scattering is present in the well
 267 ordered part of the crystal as well and interpreted as phonon scattering. Thus, the stacking sequence must consist
 268 of several layer types that have an identical structure in projection onto the \mathbf{b} axis. The easiest model that fulfills
 269 this requirement consists of identical layers shifted by some amount within the a - c -plane. As alternative model
 270 layers might be stacked that differ only slightly in the x and/or z coordinates. It is unlikely that this would not
 271 cause an additional distortion along the b -axis as well. The diffuse intensity along each rod is zero at all $h+k=0$
 272 in preservation of the extinction rule for the average structure. As pointed out earlier, the diffraction pattern can
 273 be considered the product of the diffraction pattern of a single layer with the Fourier transform of the list of layer
 274 positions. If either of these factors is zero, the diffraction pattern will be zero and no diffuse scattering will be
 275 observed. This is fulfilled, if each layer preserves the $C2/m$ symmetry, again indicating that all layer types are
 276 identical and differ by a shift in the a - c -plane only. The slices cut from three dimensional reconstructions (Fig. 7)
 277 show that no diffuse rods exist through Bragg reflections $h0l$ with $h+l$ even. This extinction rule for the diffuse
 278 scattering shows that the disorder is due to layers shifted by $\frac{1}{2}\mathbf{a} + \frac{1}{2}\mathbf{c}$. Let us denote the position of any layer
 279 within the a - c -plane as $\Delta x + \Delta z$. An ideal crystal results if this shift is zero (or identical) for all layers. The
 280 contribution to the diffraction pattern by any such layer is $(hkl) = (\sum_j^N f_j e^{2\pi i (hx_j + \Delta x) + ky_j + l(z_j + \Delta z)})^2$. The
 281 terms with Δx and Δz can be factored out to yield: $I(hkl) = (\sum_j^N f_j e^{2\pi i (hx_j + ky_j + lz_j)} e^{2\pi i (h\Delta x + l\Delta z)})^2$. If the
 282 second exponential function is equal to one, the diffraction pattern is identical to that of a perfect crystal, i.e. no
 283 diffuse scattering is present. For the exponential function to be equal to one, the term $h\Delta x + l\Delta z$ must be a whole
 284 number. As no diffuse scattering is observed for any $h+l=2n$, we can rewrite this term as $h\Delta x + (2n-h)\Delta z$ or $h(\Delta x$
 285 $- \Delta z) + 2n\Delta z$. As no diffuse scattering is observed for $h=0$ (and l even) the second term implies that $\Delta z = \frac{1}{2}$. The
 286 lack of diffuse scattering for any h in $h+l$ even in turn implies that the first term is a whole number, which
 287 requires $\Delta x = \Delta z = \frac{1}{2}$. In principal, two types of three-fold modulated disordered stacking sequences,
 288 $AAB \cdot AAB \cdot AAB$ and $ABC \cdot ABC \cdot ABC$, are imaginable. As the shift between layer types must be $\frac{1}{2}\mathbf{a} + \frac{1}{2}\mathbf{c}$, the third
 289 layer in a sequence ABC would be at an equivalent position to the initial A layer. Thus the layer sequence is
 290 restricted to AAB . A 10×10 supercell in the ac plane from the ordered crystal structure was used as basic layer
 291 type. Layer types A and B differ only by the shift $\frac{1}{2}\mathbf{a} + \frac{1}{2}\mathbf{c}$. Given this shift, the octahedral chains, as the
 292 backbone of the structure, do not change in the stacking sequence $AAB \cdot AAB$ (Fig. 6). As an alternative solution
 293 to the pure shift model, changes in the stoichiometry of layer B were tried as well. As one example of these
 294 unsuccessful trials a model with a terminal O atom (O5) suggested by Fischer *et al.* [7] was applied for B layers
 295 to build the three-fold superstructure. No strong modulated streaks in simulated diffraction patterns were
 296 observed.

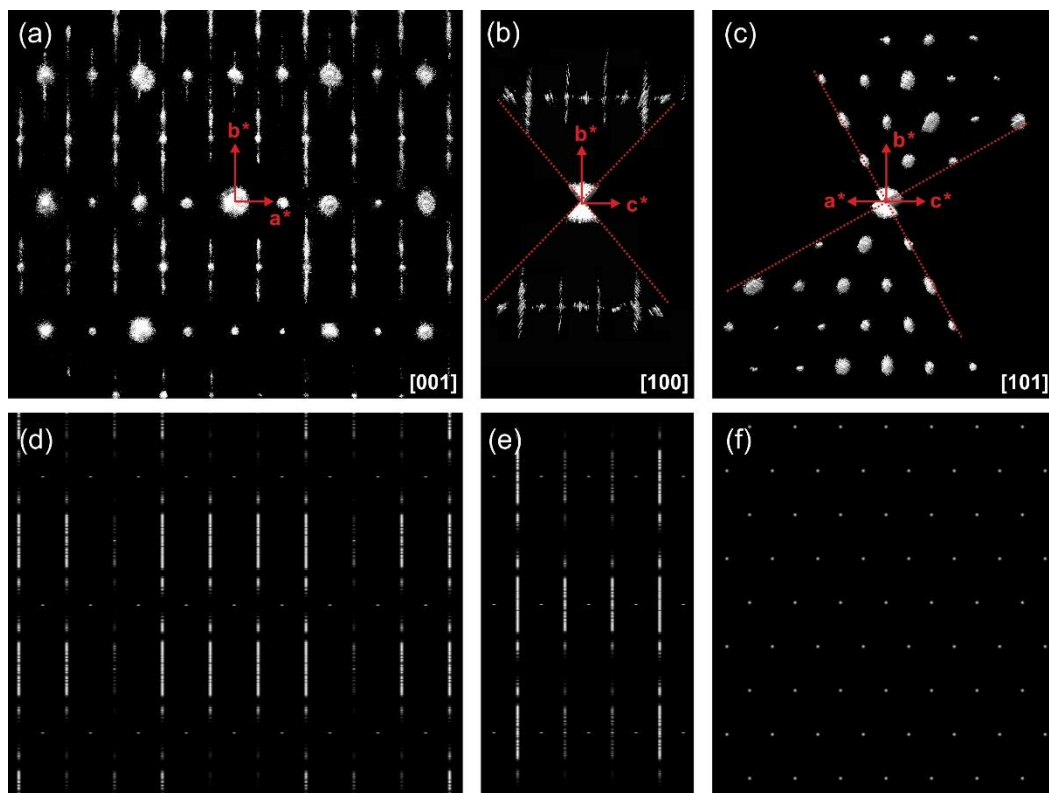


297

298 Fig. 6 Structural models used for superstructure generation. Layer A: structure solved from electron diffraction
 299 data and layer B: A with a shift of $\frac{1}{2}\mathbf{a}$ and $\frac{1}{2}\mathbf{c}$.

300 The final simulated electron diffraction patterns (zones [001], [100] and [101]) of the modelled structures
 301 describe the three-fold modulation of the \mathbf{b}^* axis and the diffuse streaks along that direction quite well (Fig. 7).
 302 In the $hk0$ and $0kl$ slices, the modulated diffuse scattering along \mathbf{b}^* axis exists for $h = 2n+1$ and $l = 2n+1$, due to
 303 the $\frac{1}{2}\mathbf{a} + \frac{1}{2}\mathbf{c}$ shift vector, whereas no diffuse scattering is present in zone [101].

304



305

306 Fig. 7 Experimental electron diffraction patterns of [001] (a), [100] (b) and [101] (c) zones cut from the
 307 reciprocal volume. (d-f): Corresponding simulated electron diffraction patterns of the three-fold superstructure.
 308 The missing cone can be observed in (b) and (c).

309

310 **Conclusion**

311 In this investigation, we demonstrated the structural characterization of $\text{Al}_4\text{B}_2\text{O}_9$ nanorods by automated
312 diffraction tomography (ADT) covering an *ab-initio* crystal structure determination of single ordered nano
313 crystals as well as high resolution TEM and HAADF-STEM imaging combined with electron diffraction
314 simulation. Reconstruction of ADT data delivered a monoclinic unit-cell in space group $C2/m$. The *ab-initio*
315 structure solution performed with direct methods from ADT data showed a well-resolved potential map
316 providing all atoms of the structure with full occupancies. The AlO_6 octahedral chains extend along the \mathbf{b} axis
317 and form the mullite-type structure framework. The chains are connected by Al-O and B-O inter-chain groups
318 forming the structural backbone. The ordered crystal structure was confirmed by TEM and HDAAF-STEM
319 imaging. For some $\text{Al}_4\text{B}_2\text{O}_9$ nanorods disorder with a three-fold modulation along the \mathbf{b} axis was observed. A
320 defective three-fold superstructure was generated by stacking ordered structure (*A*) and shifted structure (*B*)
321 along the \mathbf{b} axis. The *ac* plane of model *A* is shifted by $\frac{1}{2}\mathbf{a}$ and $\frac{1}{2}\mathbf{c}$ along the \mathbf{b} axis, resulting layer type *B*. The
322 model with a mean three-fold superstructure could be constructed by stacking the *A* and *B* layers along the \mathbf{b} axis
323 in a short range order of $\cdots\text{AAB}\cdots$. The simulated electron diffraction patterns of the constructed model are in
324 good agreement with experimental data.

325 We show that the combination of electron diffraction, imaging and simulation is a powerful tool for detailed
326 characterization of nano crystalline materials. Firstly, the complex structure of ordered single nanocrystals is
327 determined by electron diffraction tomography. Secondly, the ADT structure is confirmed by TEM and STEM
328 images along relevant zone axes. Thirdly, disorder in form of an approximate three-fold modulation is
329 constructed based on the ordered structure and electron diffraction patterns are calculated from the simulated
330 superstructure model. With this method combination addressing single nano crystals, we could elucidate the
331 structural order and disorder phenomena in mullite-type $\text{Al}_4\text{B}_2\text{O}_9$, where methods probing the bulk like X-ray or
332 neutron powder diffraction failed. Hence, it explains all crystal-chemical deficiencies observed in former crystal-
333 structure descriptions, which resulted from the superposition of ordered and disordered domains in the powder
334 material investigated by X-ray and neutron diffraction methods.

335 **Acknowledgement**

336 Haishuang Zhao gratefully acknowledges the financial support from the Carl-Zeiss-Stiftung. Yaşar Krysiak is
337 grateful for the financial support by the Stipendienstiftung Rheinland-Pfalz. Thorsten M. Gesing and Reinhard X.
338 Fischer gratefully thank the Deutsche Forschungsgemeinschaft for the financial support (GE1981/5-1 and
339 FI442/19-1). The JEM-ARM200F was partially funded by the Deutsche Forschungsgemeinschaft
340 (DFG/INST163/2951).

341 **Supporting Information**

342 **Figures:** 2D slices of $0kl$, $h0l$ and $hk0$ planes, Pawley refinement, HRSTEM overview and intensity profiles of single
343 electron nano diffraction patterns.

344 **Tables:** cell parameters from measured ADT data, refined atomic parameters and differences of atomic positions.

345

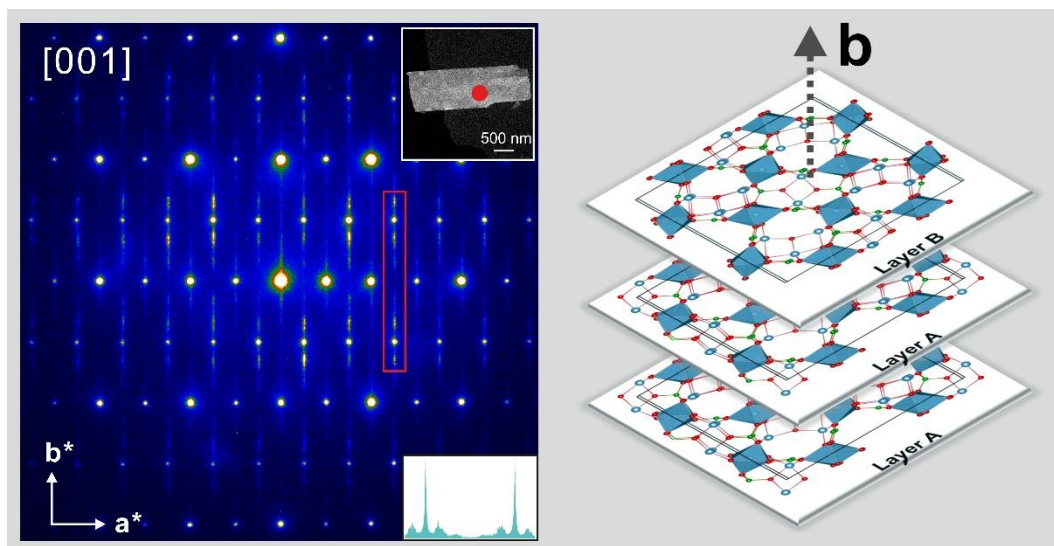
346 References

- 347 [1] Y. Huang, X. Duan, Q. Wei, C.M. Lieber, Directed assembly of one-dimensional nanostructures into functional
348 networks, *Science*. 291 (2001) 630–633. doi:10.1126/science.291.5504.630.
- 349 [2] J. Zhang, J. Lin, H.S. Song, E.M. Elssfah, S.J. Liu, J.J. Luo, X.X. Ding, C. Tang, S.R. Qi, Bulk-quantity fast production
350 of $\text{Al}_4\text{B}_2\text{O}_9/\text{Al}_{18}\text{B}_4\text{O}_{33}$ single-crystal nanorods by a novel technique, *Mater. Lett.* 60 (2006) 3292–3295.
- 351 [3] X. Tao, X. Wang, X. Li, Nanomechanical characterization of one-step combustion-synthesized $\text{Al}_4\text{B}_2\text{O}_9$ and $\text{Al}_{18}\text{B}_4\text{O}_{33}$
352 nanowires, *Nano Lett.* 7 (2007) 3172–3176. doi:10.1021/nl071772x.
- 353 [4] R.X. Fischer, H. Schneider, Crystal chemistry of borates and borosilicates with mullite-type structures: a review, *Eur. J.*
354 *Mineral.* 20 (2008) 917–933. doi:10.1127/0935-1221/2008/0020-1831.
- 355 [5] G.D. Gatta, N. Rotiroti, M. Fisch, T. Armbruster, Stability at high pressure, elastic behavior and pressure-induced
356 structural evolution of “ Al_5BO_9 ”, a mullite-type ceramic material, *Phys. Chem. Miner.* 37 (2010) 227–236.
357 doi:10.1007/s00269-009-0327-x.
- 358 [6] M. Fisch, T. Armbruster, D. Rentsch, E. Libowitzky, T. Pettke, Crystal-chemistry of mullite-type aluminoborates
359 $\text{Al}_{18}\text{B}_4\text{O}_{33}$ and Al_5BO_9 : A stoichiometry puzzle, *J. Solid State Chem.* 184 (2011) 70–80. doi:10.1016/j.jssc.2010.10.032.
- 360 [7] R.X. Fischer, V. Kahlenberg, D. Voll, K.J. MacKenzie, M.E. Smith, B. Schmetger, H.-J. Brumsack, H. Schneider,
361 Crystal structure of synthetic $\text{Al}_4\text{B}_2\text{O}_9$: A member of the mullite family closely related to boralsilite, *Am. Mineral.* 93
362 (2008) 918–927.
- 363 [8] R. Ma, Y. Bando, T. Sato, C. Tang, F. Xu, Single-crystal $\text{Al}_{18}\text{B}_4\text{O}_{33}$ microtubes, *J. Am. Chem. Soc.* 124 (2002) 10668–
364 10669. doi:10.1021/ja0271173.
- 365 [9] J. Zhang, Y. Huang, J. Lin, X.X. Ding, Z.X. Huang, S.R. Qi, C.C. Tang, From $\text{Al}_4\text{B}_2\text{O}_9$ nanowires to BN-Coated
366 $\text{Al}_{18}\text{B}_4\text{O}_{33}$ nanowires, *J. Phys. Chem. B.* 109 (2005) 13060–13062. doi:10.1021/jp052390n.
- 367 [10] D.R. Peacor, R.C. Rouse, E.S. Grew, Crystal structure of boralsilite and its relation to a family of boroaluminosilicates,
368 sillimanite, and andalusite, *Am. Mineral.* 84 (1999) 1152–1161. doi:10.2138/am-1999-7-818.
- 369 [11] H. Scholze, Über Aluminiumborate, *Z. Für Anorg. Allg. Chem.* 284 (1956) 272–277.
- 370 [12] D. Mazza, M. Vallino, G. Busca, Mullite-type structures in the systems $\text{Al}_2\text{O}_3\text{--Me}_2\text{O}$ (Me = Na, K) and $\text{Al}_2\text{O}_3\text{--B}_2\text{O}_3$, *J.*
371 *Am. Ceram. Soc.* 75 (1992) 1929–1934.
- 372 [13] K. Hoffmann, T.J.N. Hooper, H. Zhao, U. Kolb, M.M. Murshed, M. Fischer, H. Lühns, G. Nénert, P. Kudějová, A.
373 Senyshyn, H. Schneider, J.V. Hanna, T.M. Gesing, R.X. Fischer, Crystal chemical characterization of mullite-type
374 aluminum borate compounds, *J. Solid State Chem.* Submitted (2016).
- 375 [14] U. Kolb, T. Gorelik, C. Kübel, M.T. Otten, D. Hubert, Towards automated diffraction tomography: Part I—Data
376 acquisition, *Ultramicroscopy.* 107 (2007) 507–513.
- 377 [15] U. Kolb, T. Gorelik, M.T. Otten, Towards automated diffraction tomography. Part II—Cell parameter determination,
378 *Ultramicroscopy.* 108 (2008) 763–772.
- 379 [16] E. Mugnaioli, I. Andrusenko, T. Schüler, N. Loges, R.E. Dinnebier, M. Panthöfer, W. Tremel, U. Kolb, Ab Initio
380 structure determination of vaterite by automated electron diffraction, *Angew. Chem. Int. Ed.* 51 (2012) 7041–7045.
381 doi:10.1002/anie.201200845.
- 382 [17] T.E. Gorelik, C. Czech, S.M. Hammer, M.U. Schmidt, Crystal structure of disordered nanocrystalline α^{II} -quinacridone
383 determined by electron diffraction, *CrystEngComm.* 18 (2016) 529–535. doi:10.1039/C5CE01855B.
- 384 [18] K. Hoffmann, M.M. Murshed, R.X. Fischer, H. Schneider, T.M. Gesing, Synthesis and characterization of mullite-type
385 $(\text{Al}_{1-x}\text{Ga}_x)_4\text{B}_2\text{O}_9$, *Z. für Krist.-Cryst. Mater.* 229 (2014) 699–708.
- 386 [19] A. Coelho, Coelho Software, TOPAS Acad. User Man. (2007) Brisbane, Australia.
- 387 [20] E. Mugnaioli, T. Gorelik, U. Kolb, “Ab initio” structure solution from electron diffraction data obtained by a
388 combination of automated diffraction tomography and precession technique, *Ultramicroscopy.* 109 (2009) 758–765.
389 doi:10.1016/j.ultramic.2009.01.011.
- 390 [21] R. Vincent, P.A. Midgley, Double conical beam-rocking system for measurement of integrated electron diffraction
391 intensities, *Ultramicroscopy.* 53 (1994) 271–282. doi:10.1016/0304-3991(94)90039-6.
- 392 [22] C.T. Koch, Determination of core structure periodicity and point defect density along dislocations, PhD Thesis. (2002).
- 393 [23] Barton et al., *Ultramicroscopy.* (2016) under review.
- 394 [24] J. Barthel, Dr. Probe - High-resolution (S)TEM image simulation software, (2016). <http://www.er-c.org/barthel/drprobe/>.
- 395 [25] M.C. Burla, R. Caliendo, B. Carrozzini, G.L. Cascarano, C. Cuocci, C. Giacovazzo, M. Mallamo, A. Mazzone, G.
396 Polidori, Crystal structure determination and refinement via *SIR2014*, *J. Appl. Crystallogr.* 48 (2015) 306–309.
397 doi:10.1107/S1600576715001132.
- 398 [26] G.M. Sheldrick, SHELX-97, program for the solution and refinement of crystal structures, (1997). University of
399 Göttingen, Germany.
- 400 [27] K. Momma, F. Izumi, VESTA 3 for three-dimensional visualization of crystal, volumetric and morphology data, *J. Appl.*
401 *Crystallogr.* 44 (2011) 1272–1276. doi:10.1107/S0021889811038970.
- 402 [28] T. Proffen, R.B. Neder, DISCUS: a program for diffuse scattering and defect-structure simulation, *J. Appl. Crystallogr.*
403 30 (1997) 171–175.
- 404
- 405
- 406
- 407
- 408

409 **Highlights:**

- 410 1. *Ab-initio* structure solution by electron diffraction from single nanocrystals.
411 2. Detected modulation corresponding mainly to three-fold superstructure.
412 3. Diffuse diffraction streaks caused by stacking faults in disordered crystals.
413 4. Observed streaks explained by simulated electron diffraction patterns.

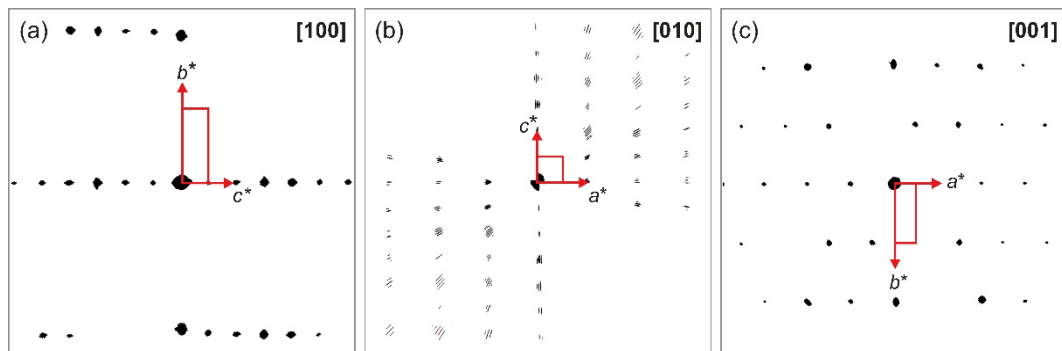
414 **Graphical abstract:**



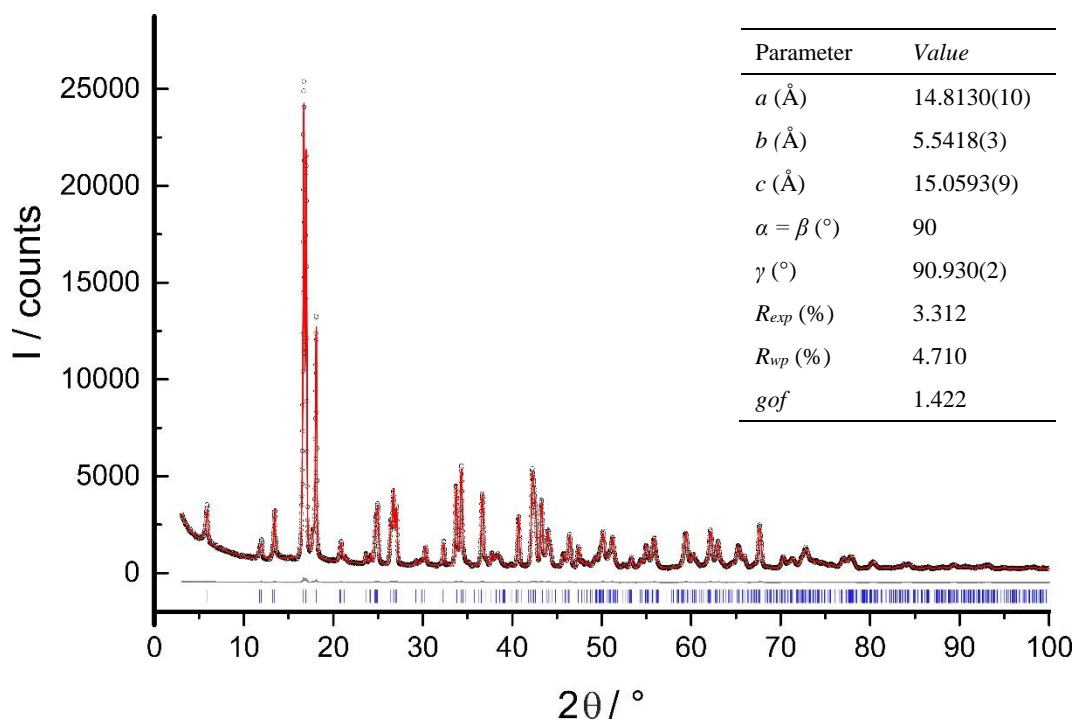
415

416

417 Supporting information

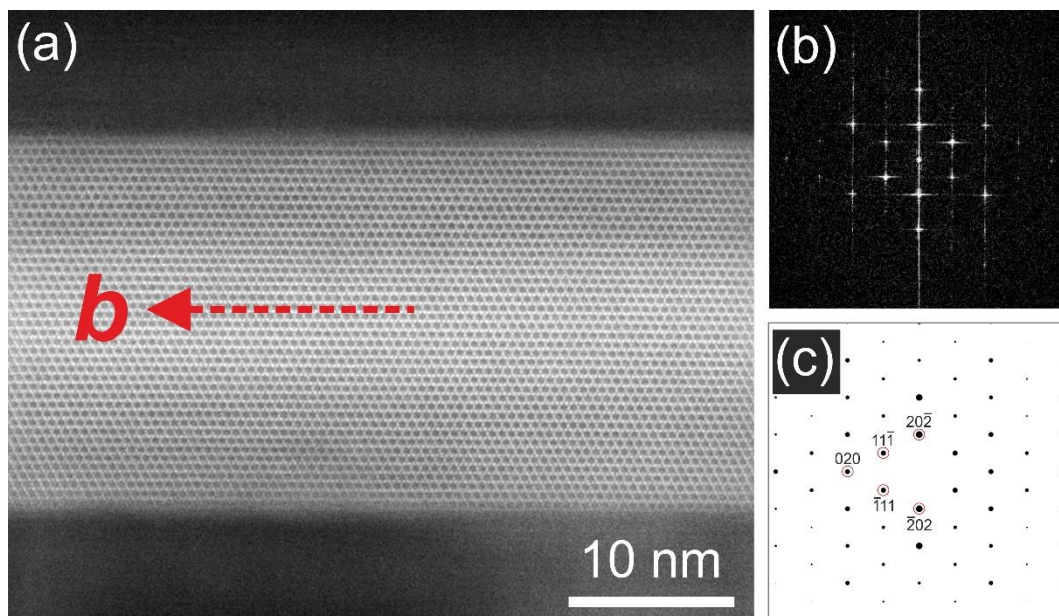


418
419 Fig. S1 Two-dimensional slice cut from reconstructed 3D reciprocal space: (a) $0kl$, (b) $h0l$ and (c) $hk0$ planes.



436 Fig. S2 Pawley fit plot of $Al_4B_2O_9$. Observed powder diagram (black circles), simulated powder diagram (red
437 solid line), difference profiles (grey solid line), and reflection positions (blue vertical lines).

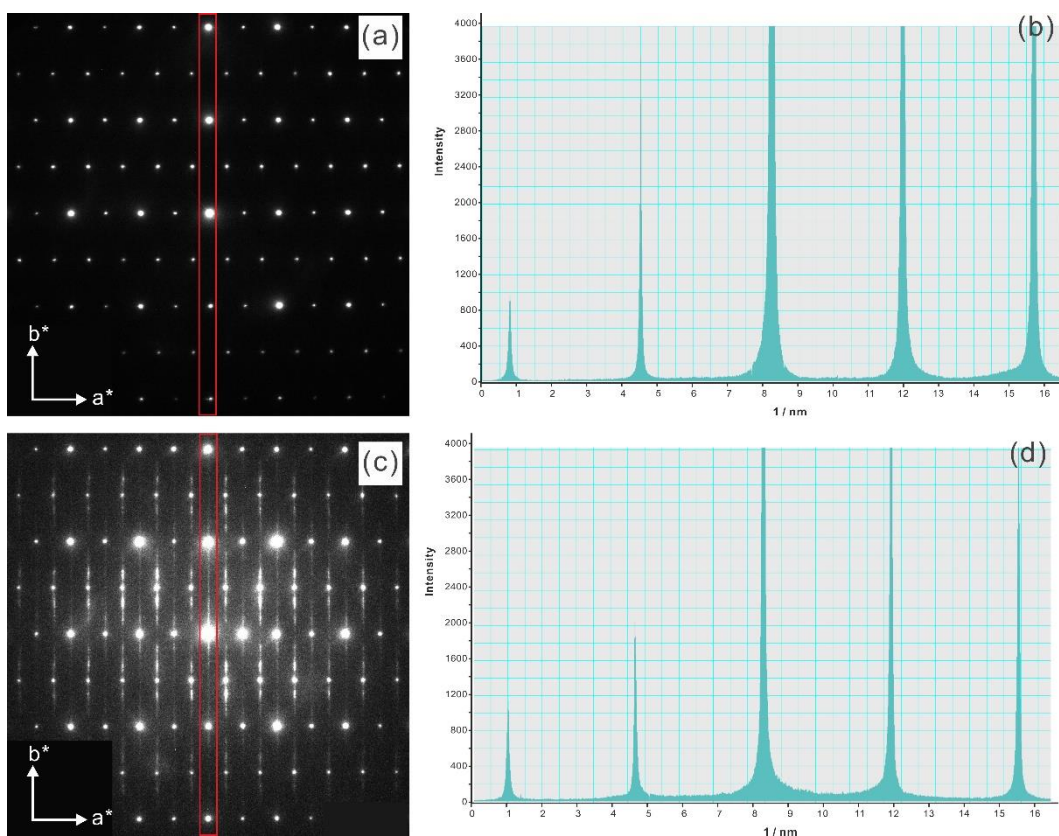
438



439

440 Fig. S3 (a) HDAAF-HRSTEM overview taken along the [101] zone, (b) its corresponding FFT image and (c)
 441 simulated electron diffraction pattern of $\text{Al}_4\text{B}_2\text{O}_9$ along [101] zone axis. HRSTEM shows that the nanorods grow
 442 along the crystallographic b axis.

443



444

445 Fig. S4 (a, c) Single electron nano diffraction patterns recorded from different regions of a $\text{Al}_4\text{B}_2\text{O}_9$ crystallite
 446 oriented in [001] direction. (b) and (d): Intensity profiles taken along respective $0k0$ remarked diffraction lines in
 447 (a) and (c).

448

449 Table S1 Cell parameters from measured ADT data and from Pawley fit of XRPD data for comparison.

	<i>a</i> (Å)	<i>b</i> (Å)	<i>c</i> (Å)	α (°)	β (°)	γ (°)	Precession
<i>CryI</i>	14.66	5.54	15.21	89.2	90.7	89.4	No
<i>CryII</i>	14.61	5.49	15.41	89.8	92.1	91.4	No
<i>CryIII</i>	14.89	5.55	14.96	89.9	89.9	89.9	No
<i>CryIV</i>	14.77	5.58	14.99	90.5	91.1	90.3	No
Mean (no Precession)	14.73	5.54	15.14	89.9	90.9	90.3	
XRPD	14.81	5.54	15.17	90.0	90.9	90.0	
<i>CryV</i>	14.61	5.57	15.18	87.9	90.8	88.8	Yes
<i>CryVI (Dataset I)</i>	14.91	5.48	15.12	90.3	91.3	90.1	Yes
<i>CryVI (Dataset II)</i>	14.68	5.52	15.24	90.6	91.4	90.5	Yes
<i>Cry VII</i>	14.90	5.45	15.23	89.7	92.1	88.7	Yes

450

451 Table S2 Refined atomic parameters of ordered Al₄B₂O₉ structure refined from ADT data and corresponding
452 parameters from XRPD in the literature of Fischer *et al.*[7].

Site	Wyck. posit.	x		y		z		U _{iso} (Å ²)		Occupancy		Difference (Å)
		ADT	XRPD	ADT	XRPD	ADT	XRPD	ADT	XRPD	ADT	XRPD	
Al1	4i	0.8627(8)	0.8631(6)	0	0	0.3351(8)	0.3409(6)	0.018(3)	0.005(1)	1	1	0.0058
Al2	4i	0.8094(10)	0.8147(6)	0	0	0.1556(9)	0.1622(6)	0.029(3)	0.005(1)	1	1	0.0085
Al3	4i	0.5732(11)	0.5696(6)	0	0	0.0729(11)	0.0675(6)	0.033(4)	0.005(1)	1	1	0.0065
Al4	4i	0.6699(11)	0.6739(7)	0	0	0.3426(10)	0.3439(6)	0.030(4)	0.005(1)	1	1	0.0042
Al5	8j	0.0007(4)	0.0002(6)	0.7411(13)	0.7471(16)	0.2425(5)	0.2480(5)	0.010(2)	0.005(1)	1	1	0.0082
Al6	4e	¼	¼	¼	¼	0	0	0.024(3)	0.005(1)	1	1	0
Al7	4f	¼	¼	¼	¼	½	½	0.029(3)	0.005(1)	1	1	0
B1	4i	0.1029(16)	0.1026(20)	0	0	0.1078(16)	0.1053(19)	0.010(5)	0.005(1)	1	1	0.0025
B2	4i	0.3762(14)	0.3789(23)	0	0	0.1144(14)	0.1382(21)	0.042(9)	0.005(1)	1	1	0.0240
B3	4i	0.1252(2)	0.1352(25)	0	0	0.3708(2)	0.3662(20)	0.036(8)	0.005(1)	1	1	0.0113
B4	4i	0.3874(16)	0.3896(22)	0	0	0.3880(17)	0.4005(19)	0.021(6)	0.005(1)	1	1	0.0127
O1	4i	0.7618(14)	0.7563(13)	0	0	0.2670(12)	0.2561(10)	0.033(5)	0.009(1)	1	1	0.0122
O2	4i	0.7873(14)	0.7979(11)	0	0	0.4338(12)	0.4445(10)	0.037(5)	0.009(1)	1	1	0.0151
O3	4i	0.9180(14)	0.9245(12)	0	0	0.2233(12)	0.2152(8)	0.031(5)	0.009(1)	1	1	0.0104
O4	8j	0.9219(8)	0.9226(6)	0.7120(2)	0.7157(20)	0.3560(8)	0.3536(6)	0.021(3)	0.009(1)	1	1	0.0044
O5	4i		0.0332(19)		0		0.4376(16)		0.009(1)	0	0.5	
O6	4i	0.3190(9)	0.3221(11)	0	0	0.4507(10)	0.4562(10)	0.010(3)	0.009(1)	1	1	0.0063
O7	8j	0.8183(8)	0.8261(7)	0.7049(2)	0.7183(18)	0.1041(8)	0.0993(5)	0.023(3)	0.009(1)	1	1	0.0161
O8	4i	0.6965(12)	0.6967(12)	0	0	0.0578(12)	0.0682(9)	0.022(4)	0.009(1)	1	1	0.0104
O9	8j	0.0679(8)	0.0663(7)	0.7774(3)	0.7711(22)	0.1367(9)	0.1310(6)	0.022(3)	0.009(1)	1	1	0.0083
O10	4i	0.4431(13)	0.4300(20)	0	0	0.0485(13)	0.0474(19)	0.035(5)	0.009(1)	1	0.5	0.0132
O11	8j	0.6611(9)	0.6734(6)	0.2822(3)	0.2852(20)	0.4047(10)	0.3953(5)	0.031(3)	0.009(1)	1	1	0.0157
O12	4i	0.5746(11)	0.5766(12)	0	0	0.2763(12)	0.2751(9)	0.020(4)	0.009(1)	1	1	0.0023
O13	4i	0.4255(10)	0.4362(11)	0	0	0.1950(10)	0.1981(9)	0.015(3)	0.009(1)	1	1	0.0111
O14	4i	0.0691(13)	0.0659(11)	0	0	0.3023(12)	0.2919(9)	0.023(4)	0.009(1)	1	1	0.0108
O15	4i	0.8341(11)	0.8242(10)	0	0	0.9615(11)	0.9558(10)	0.018(4)	0.009(1)	1	1	0.0114
Max. of Error		0.0016	0.0025	0.0013	0.0022	0.0017	0.0021	0.009	0.001			

453 Table S3 Differences of the atomic positions in the structures refined from ADT data and XRPD data.

	Al	O	B
Mean (Å)	0.005	0.011	0.013
Maximum (Å)	0.009	0.016	0.024

454